SOILS AND FOUNDATIONS Vol. 29. No. 4, 1-13, Dec. 1989
Japanese Society of Soil Mechanics and Foundation Engineering

SHEAR BANDS FORMATION NUMERICALLY SIMULATED BY A NON-COAXIAL CAM-CLAY MODEL

CHIKAYOSHI YATOMI[i], ATSUSHI YASHIMA[ii], ATSUSHI IIZUKA[iii] and IKUO SANO[iv]

ABSTRACT

This paper is concerned with the formation of the shear bands by employing the finite element method with a non-coaxial Cam-clay model developed in our last paper (Yatomi et al., 1989). This finite element method for finite strains is formulated as a soil/water coupling form based on the updated Lagrangean scheme. A demonstration of shear bands formation is given in a classical rigid punch problem without introducing any initial imperfections into the material elements.

Key words : bearing capacity, elasto-plastic, finite element method, finite strain, localization of deformation, saturated ground, shear bands (**IGC** : E 3/D 6)

INTRODUCTION

In our last paper (Yatomi et al., 1989), we presented a non-coaxial Cam-clay model for finite strains in order to study the formation of localized shear bands. In this paper, we first give the finite element formulation based on the updated Lagrangean scheme. We then demonstrate shear bands formation with a rigid punch problem.

The finite element method is formulated as a soil/water coupling form initiated by Biot (1956) for small strains, in which we may consider the interaction between the deformation of soils and the flow of pore water. The equilibrium equation is, as usual, discretized based on the principle of virtual work, and the continuity condition of the pore water is discretized in the form of the finite difference approximation, which was initiated by Christian (1968) and Christian and Boehmer (1970). The finite element program developed here for the shear bands analysis has been named SHEBLA (SHEar Band Localization Analysis). The accuracy of SHEBLA can be demonstrated by a few simple examples.

Under undrained plane strain conditions, SHEBLA is applied to a rigid punch problem to simulate the formation of localized shear bands. The results show that shear band localization takes place as both the deforma-

i) Instructor, Dept. of Aeronautical Eng., Kyoto University, Kyoto 606.
ii) Instructor, Disaster Prevention Research Institute, Kyoto University, Uji, Kyoto 611.
iii) Instructor, Dept. of Civil Eng., Kanazawa University, Kanazawa 920.
iv) Instructor, Dept. of Civil Eng., Kyoto University, Kyoto 606.
Manuscript was received for review on May 11, 1988.
Written discussions on this paper should be submitted before July 1, 1990, to the Japanese Society of Soil Mechanics and Foundation Engineering, Sugayama Bldg. 4F, Kanda Awaji-cho 2-23, Chiyoda-ku, Tokyo 101, Japan. Upon request the closing date may be extended one month.

tion of finite element meshes and also as localized strain distributions ; the computed pattern of deformation is very similar to the classical slip line solution. It should be noted that no initial imperfections are introduced here in the material elements ; and hence, the development of the shear bands is not artificial (cf. Prevost, 1984).

After examining the bearing capacity, we shall discuss the trajectory path in the characteristic regimes and the effective stress path in the stress space for five typical material elements. Finally, we will obtain the distribution of the footing stress.

GOVERNING EQUATIONS

We will first summarize the governing equations, which are the bases of our finite element formulation in the soil/water coupling form, and then briefly review the constitutive model.

Governing Equations

Assuming Darcy's law to describe the pore water flow, the basic governing equations are summarized as follows (for details, see Yatomi et al., 1989 and Biot, 1956) :

a) continuing equilibrium equation

$$div\,\dot{\boldsymbol{S}}_t=\boldsymbol{0}$$

b) effective stress concept $\boldsymbol{T}=\boldsymbol{T}'-u\,\boldsymbol{1}$

c) constitutive equation $\mathring{\boldsymbol{T}}'=\mathcal{L}[\boldsymbol{D}]$ (1)

d) continuity condition of pore water

$$tr\,\boldsymbol{D}=\boldsymbol{K}\cdot\mathrm{grad}(\mathrm{grad}\ h_w) \qquad (2)$$

e) water head $h_w=u/\gamma_w+\Omega$ (3)

with the appropriate boundary conditions and the initial conditions.

Here, $\dot{\boldsymbol{S}}_t$ is the total nominal stress-rate, $\boldsymbol{T}$ is the Cauchy stress tensor, $\boldsymbol{T}'$ is the effective stress tensor, u is the pore water pressure, $\mathring{\boldsymbol{T}}'$ is the co-rotational rate of effective stress, $\boldsymbol{D}$ is the stretching, $\boldsymbol{K}$ is the permeability tensor, h_w is the total head of pore water, γ_w is the unit weight of pore water, and Ω is the potential head. Note here that we regard both tension and extension as positive, and both compression and contraction as negative, except u, p', and the volumetric strain. Assuming that permeability tensor $\boldsymbol{K}$ is isotropic, we may write $\boldsymbol{K}=k\,\boldsymbol{1}$, where k is called the coefficient of permeability. When considering anisotropy of $\boldsymbol{K}$, we may express $\boldsymbol{K}$ as $\boldsymbol{K}=k_{ij}(\boldsymbol{b}_i\otimes\boldsymbol{b}_j)$, where $\boldsymbol{b}_i$ $(i=1, 2, 3)$ are the reference unit vectors whose directions correspond to the principal axes of anisotropy (see Yatomi and Nishihara, 1984).

Constitutive Equation

The constitutive stiffness tensor of the coaxial Cam-clay model for finite strains is denoted as

$$\mathcal{L}_{ijkl}=\left(\tilde{K}-\frac{2}{3}\tilde{G}\right)\delta_{ij}\delta_{kl}+\tilde{G}(\delta_{ik}\delta_{jl}+\delta_{il}\delta_{jk}) -\frac{\left(\frac{\tilde{G}}{\bar{\tau}}S_{ij}-\bar{\beta}\tilde{K}\delta_{ij}\right)\left(\frac{\tilde{G}}{\bar{\tau}}S_{kl}-\bar{\beta}\tilde{K}\delta_{kl}\right)}{\tilde{G}+\bar{\beta}^2\tilde{K}+h}, \qquad (4)$$

where $\tilde{K}=\dfrac{1+e}{\kappa}p'$, $\tilde{G}=\dfrac{3(1-2\nu)}{2(1+\nu)}p'$,

$$\bar{\beta}=\frac{1}{\sqrt{3}}(M-\eta),\quad \bar{\tau}=\frac{1}{\sqrt{2}}\|\boldsymbol{S}\|,$$

$$\eta=\sqrt{3}\frac{\bar{\tau}}{p'},\ \text{and}\ h=\frac{\bar{\beta}}{\sqrt{3}D}p'.$$

Material parameters D, M, κ, and ν are the coefficient of dilatancy, the critical state parameter, the swelling index, and the Poisson's ratio in terms of effective stress, respectively. Also, e is the void ratio, p' is the effective mean stress $(=-tr\boldsymbol{T}'/3)$, and $\boldsymbol{S}$ is the deviatoric stress tensor $(=\boldsymbol{T}'+p'\boldsymbol{1})$. In order to obtain non-coaxial Cam-clay model we need only introduce the following transformation :

$$\tilde{G}\longrightarrow\frac{h_1\tilde{G}}{h_1+\tilde{G}},$$

$$h\longrightarrow\frac{hh_1}{h_1-h},$$

$$\tilde{K}\longrightarrow\frac{\tilde{K}}{1-\tilde{K}\bar{\beta}^2/(h_1-h)},$$

$$\text{and}\ \ \bar{\beta}\longrightarrow\frac{h_1\bar{\beta}}{h_1-h},$$

where h_1 is the second hardening modulus

defined as $\frac{\bar{\beta}}{\sqrt{3}A}p'$ with a positive material constant, A. For further details, please refer to Yatomi et al., 1989.

FINITE ELEMENT FORMULATION

The coupling problem which considers the interaction of soil/water is formulated for application as a simultaneous system of equations consisting of the equilibrium equation which is discretized based on the principle of virtual work and the continuity condition which is discretized in the form of the finite difference approximation originally developed by Christian (1968) (cf. Akai and Tamura, 1978 ; Iizuka and Ohta, 1987).

Discretization of Equilibrium Equation

The principle of virtual work is expressed as :

$$\int_v \dot{\boldsymbol{S}}_t \cdot \delta \boldsymbol{L} dv = \int_a \dot{\boldsymbol{s}} \cdot \delta \boldsymbol{v} da, \qquad (5)$$

where $\boldsymbol{L}$ is the velocity gradient, $\dot{\boldsymbol{s}}$ is the total nominal traction-rate, and $\boldsymbol{v}$ is the velocity vector.

Substituting

$$\dot{\boldsymbol{S}}_t = \dot{\boldsymbol{S}}_t' - \dot{u}\,\mathbf{1} - u(tr\boldsymbol{D})\mathbf{1} + u\boldsymbol{L}^T$$

with

$$\dot{\boldsymbol{S}}_t' = \mathring{\boldsymbol{T}}' + \boldsymbol{T}'(tr\boldsymbol{D}) - (\boldsymbol{T}'\boldsymbol{D} + \boldsymbol{D}\boldsymbol{T}') + \boldsymbol{L}\boldsymbol{T}'$$

in Eq. (5), we have

$$\begin{aligned}\int_v \{&\mathring{\boldsymbol{T}}' \cdot \delta \boldsymbol{D} + \boldsymbol{T}'(tr\boldsymbol{D}) \cdot \delta \boldsymbol{D} - (\boldsymbol{T}'\boldsymbol{D} + \boldsymbol{D}\boldsymbol{T}') \cdot \delta \boldsymbol{L} \\ &+ \boldsymbol{L}\boldsymbol{T}' \cdot \delta \boldsymbol{L} - u(tr\boldsymbol{D})(tr\delta \boldsymbol{D})\mathbf{1} \\ &+ u\boldsymbol{L}^T \cdot \delta \boldsymbol{L}\} dv - \int_v \dot{u}(tr\delta \boldsymbol{D})\mathbf{1} dv \\ &= \int_a \dot{\boldsymbol{s}} \cdot \delta \boldsymbol{v} da. \end{aligned} \qquad (6)$$

We note that under undrained conditions, the terms with $tr\boldsymbol{D}$ in Eq. (6) vanish.

We express the velocity field inside an element as

$$\{v\} = [N]\{v^N\},$$

where $[N]$ is called the shape matrix and $\{v^N\}$ is the velocity at a nodal point.

Differentiating matrix $[N]$, we obtain the stretching and velocity gradient inside an element as :

$$\{D\} = [B]\ \{v^N\}, \qquad (7)$$

$$\text{and } \{L\} = [M]\{v^N\}. \qquad (8)$$

On the other hand, the volume change is presented by rearranging Eq. (7) to read

$$tr\boldsymbol{D} = [B_v]\{v^N\}. \qquad (9)$$

The change of potential head at the gravity center z_G of the element is estimated as

$$\gamma_w \dot{Q} = \gamma_w \dot{z}_G = [B_G]\{v^N\}. \qquad (10)$$

Substituting Eqs. (7), (8), and (9) into Eq. (6), the stiffness matrix equation for an element yields :

$$\begin{aligned}\Big\{&\int_v [B]^T[C][B]dv + \int_v [B]^T[T']^*[B_v]dv \\ &-2\int_v [B]^T[T']^{**}[B]dv \\ &+\int_v [M]^T[T']^{***}[M]dv - \int_v [B_v]^T u [B_v]dv \\ &+\int_v [M]^T[U]^*[M]dv\Big\}\{v^N\} - \int_v [B_v]^T \dot{u} dv \\ &= \int_a [N]^T\{\dot{s}\}da, \end{aligned} \qquad (11)$$

where $[C]$ is the constitutive stiffness matrix corresponding to Eq. (4). Hereafter, to simplify our analysis, we shall limit our discussion to the case under plane strain condition. Each term in Eq. (11) reduces to ;

$$\{D\} = \begin{Bmatrix} D_{11} \\ D_{22} \\ 2D_{12} \end{Bmatrix}, \quad \{L\} = \begin{Bmatrix} L_{11} \\ L_{22} \\ L_{12} \\ L_{21} \end{Bmatrix}, \quad \{T'\} = \begin{Bmatrix} T'_{11} \\ T'_{22} \\ T_{12} \\ T'_{33} \end{Bmatrix},$$

$$\{T'\}^* = \begin{Bmatrix} T'_{11} \\ T'_{22} \\ T_{12} \end{Bmatrix},$$

$$[T']^{**} = \begin{bmatrix} T'_{11} & 0 & T_{12}/2 \\ 0 & T'_{22} & T_{12}/2 \\ T_{12}/2 & T_{12}/2 & (T'_{11}+T'_{22}/2 \end{bmatrix},$$

$$[T']^{***} = \begin{bmatrix} T'_{11} & 0 & T_{12} & 0 \\ 0 & T'_{22} & 0 & T_{12} \\ T_{12} & 0 & T'_{22} & 0 \\ 0 & T_{12} & 0 & T'_{11} \end{bmatrix},$$

$$[U]^* = \begin{bmatrix} u & 0 & 0 & 0 \\ 0 & u & 0 & 0 \\ 0 & 0 & 0 & u \\ 0 & 0 & u & 0 \end{bmatrix},$$

$$[C]=\begin{bmatrix} \mathcal{L}_{1111} & \mathcal{L}_{1122} & \mathcal{L}_{1112} \\ \mathcal{L}_{2211} & \mathcal{L}_{2222} & \mathcal{L}_{2212} \\ \mathcal{L}_{1211} & \mathcal{L}_{1222} & \mathcal{L}_{1212} \\ \mathcal{L}_{3311} & \mathcal{L}_{3322} & \mathcal{L}_{3312} \end{bmatrix}.$$

We can ignore the second and fifth terms at the left hand side of Eq. (11) under undrained conditions ($tr\boldsymbol{D}=0$).

Substituting the time differentiation of Eq. (3) into Eq. (11), we finally obtain the following incremental form for Eq. (11), using Euler's difference approximation between $t=t$ and $t=t+\Delta t$:

$$\{[K_1]+[K_2]-2[K_3]+[K_4]-[K_5]+[K_6]+[K_v][B_G]\}|_t\{\Delta d\}-[K_v]|_t\gamma_w h_w{}^e|_{t+\Delta t}=\{\Delta F\}-[K_v]|_t\gamma_w h_w{}^e|_t, \quad (12)$$

where the total water head, h_w, is used as a variable in this paper rather than the pore water pressure, u, which is converted into h_w by Eq. (10), i.e., $u^e=\gamma_w h_w{}^e-\gamma_w z_G$ from Eq. (3), and then, $\Delta u^e=\gamma_w h_w{}^e|_{t+\Delta t}-\gamma_w h_w{}^e|_t-\Delta t\gamma_w \dot{z}_G$. The superscript e on h_w stands for the value at the gravity center of an element. In Eq. (12) we write

$$[K_1]=\int_v [B]^T[C][B]dv,$$

$$[K_2]=\int_v [B]^T[T']^*[B_v]dv,$$

$$[K_3]=\int_v [B]^T[T']^{**}[B]dv,$$

$$[K_4]=\int_v [M]^T[T']^{***}[M]dv,$$

$$[K_5]=\int_v [B_v]^T u[B_v]dv,$$

$$[K_6]=\int_v [M]^T[U]^*[M]dv,$$

$$[K_v]=\int_v [B_v]^T dv,$$

$$\{\Delta F\}=\int_a [N]^T\{\dot{s}\}\Delta t da,$$

and $\{\Delta d\}=\{v^N\}\Delta t$ is the increment of nodal displacements.

Eq. (12) is formulated incrementally, which can be regarded as Euler's forward difference. Such a discretized equation is ready to be applied to the coupling form as explained in the next section. This calculation procedure, however, requires time interval (Δt) which is small enough not to diverge. In our numerical simulation, we solve Eq. (12) stepwise under given boundary and initial conditions without introducing any iterative techniques such as the Newton-Raphson's procedure. The major advantage of adopting this calculation scheme based on Euler's forward difference method is its simplicity in making the first trial of simulation for shear bands formation in soil materials easy to understand, even in the cases where the pore water flow is coupled. The improvement of this calculation technique which aims at solving the finite strain-coupling problem more economically and exactly shall be the future target of our investigations.

Discretization of Continuity Condition

Consider an element M surrounded by elements M1, M2, M3, and M4 (Fig. 1). Here, and in what follows, we shall assume the isotropy for the permeability tensor, i.e., $\boldsymbol{K}=k\boldsymbol{1}$. Integrating Eq. (2) over by ment M and using the divergence theorem, we get :

$$\int_v tr\boldsymbol{D}dv=k\int_a (\mathrm{grad}\, h_w)\cdot\boldsymbol{n}da, \quad (13)$$

where $\boldsymbol{n}$ is an outward unit normal vector to the element M. Using the backward finite

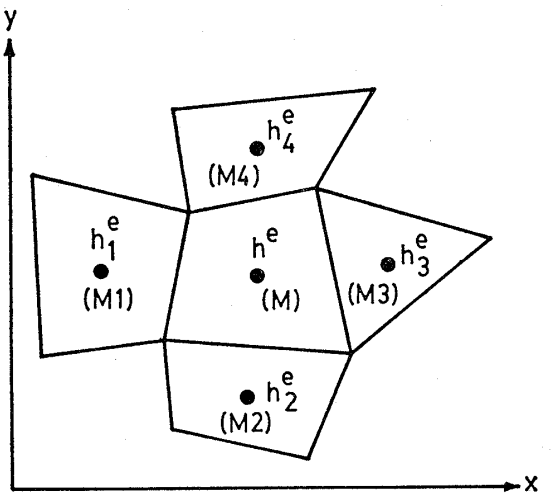

Fig. 1. Element M and its neighboring elements

differential scheme, we rewrite the right hand side of Eq. (13) as :

$$k\int_a \text{grad}\, h_w|_{t+\Delta t}\cdot \boldsymbol{n}da = \frac{1}{\Delta t}(\alpha\gamma_w h_w{}^e|_{t+\Delta t} - \sum_i \alpha_i\gamma_w h_w{}^e{}_i|_{t+t\Delta}), \quad (14)$$

where

$$\alpha=\sum_i \frac{k\Delta t}{\gamma_w}\cdot\frac{\int_a dy_i}{x_G-x_{Gi}}-\sum_i\frac{k\Delta t}{\gamma_w}\cdot\frac{\int_a dx_i}{y_G-y_{Gi}},$$

$$\alpha_i=\frac{k\Delta t}{\gamma_w}\cdot\frac{\int_a dy_i}{x_G-x_{Gi}}-\frac{k\Delta t}{\gamma_w}\cdot\frac{\int_a dx_i}{y_G-y_{Gi}},$$

and $(x_G,\ y_G)$ and $(x_{Gi},\ y_{Gi})$ are the coordinates at the gravity center of element M and its neighboring elements, respectively.

On the other hand, using Eq. (9), the left hand side of Eq. (13) is rewritten as :

$$\int_v tr\boldsymbol{D}dv=\left(\int_v [B_v]dv\right)\{v^N\}=[K_v]^T\{v^N\} =[K_v]^T|_t\{\Delta d\}/\Delta t. \quad (15)$$

Substituting Eqs. (14) and (15) into Eq. (13), we get the final form for the continuity condition, namely,

$$[K_v]|_t\{\Delta d\}=\alpha\gamma_w h_w{}^e|_{t+\Delta t}-\sum_i \alpha_i\gamma_w h_w{}^e|_{t+\Delta t}. \quad (16)$$

Combining Eqs. (12) and (16), we finally obtain the finite element formulation for a coupled problem as

$$\begin{bmatrix}[K] & -[K_v]\\ -[K_v]^T & \alpha\end{bmatrix}_t\cdot\begin{Bmatrix}\{\Delta d\}\\ \gamma_w h_w{}^e|_{t+\Delta t}\end{Bmatrix} -\begin{Bmatrix}\{0\}\\ \sum_i \alpha_i\gamma_w h_w{}^e{}_i|_{t+\Delta t}\end{Bmatrix}=\begin{Bmatrix}\{\Delta F\}-[K_v]\gamma_w h_w{}^e|_t\\ 0\end{Bmatrix}, \quad (17)$$

where $[K]=[K_1]+[K_2]-2[K_3]+[K_4]-[K_5]+[K_6]+[K_v]\,[B_G]$. The finite element program based on Eq. (17) is named SHEBLA (SHEar Band Localization Analysis). For later analyses, we will only consider the undrained behavior and will neglect the change in potential head ; therefore, $[K_2]$ $[K_5]$, $[K_v]$, α, and $\alpha_i (i=1\sim4)$ in Eq. (17) vanish.

However, the over-constraint condition should definitely be avoided. This condition arises when the number of unknown values is less than the number of discretized simultaneous equations represented by Eq. (17). The continuity equation, Eq. (16), under incompressibility conditions plays a rule as the constraint condition on the equilibrium equation of Eq. (12) (see Nagtegaal et al., 1974 ; Kikuchi, 1983). In SHEBLA, therefore, we employ the linear interpolation function to discretize, spatially, the velocity field in a quadrilateral finite element. We also define the pore water head discretely at the center of an element.

DEMONSTRATION OF ACCURACY OF SHEBLA

To verify the accuracy of the numerical method proposed here, we shall compare the numerical results with the theoretical ones in the simple laboratory tests under undrained conditions (Fig. 2). Figs. 3(a) shows the stress strain relations and effective stress paths for both coaxial and non-coaxial ($A=0.01$) Cam-clay models in the case of unconfined compression test. Results obtained through use of the finite element method coincide very well with the theoretical results for both coaxial and non-coaxial models. In the case of plane strain compression, the results for the non-coaxial model coincide with those for the coaxial model. Fig. 3(b) shows a comparison in the case of simple shear test. The numerical results also agree rather well with those obtained from theory.

These demonstrations confirm the useful-

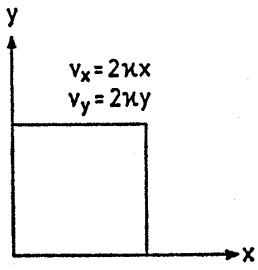

Fig. 2(a) Unconfined compression test

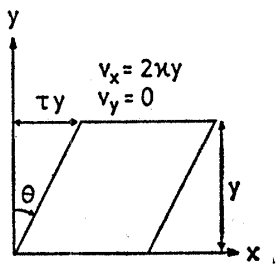

Fig. 2(b) Simple shear test

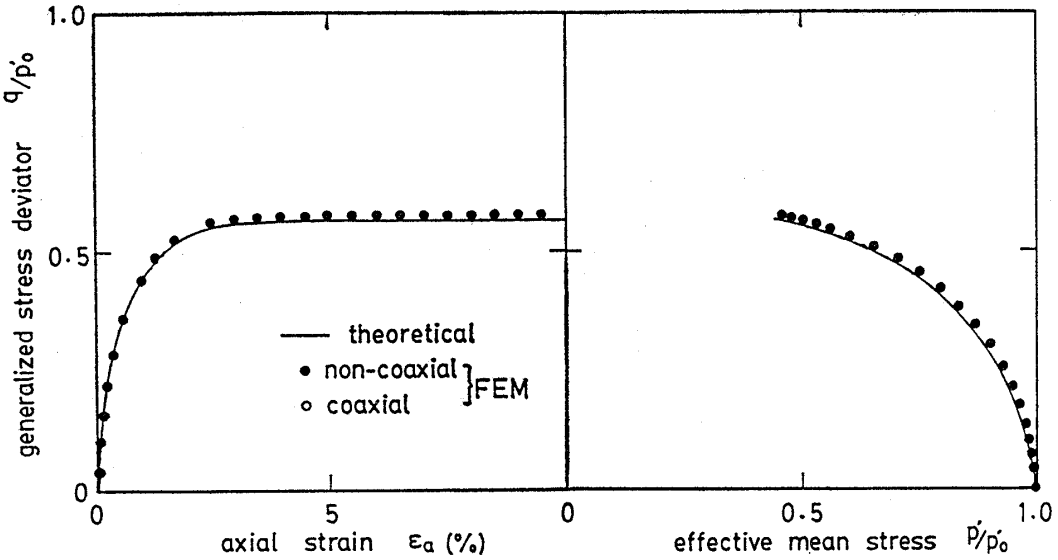

Fig. 3(a). The stress-strain relations and the effective stress path for an unconfined compression test

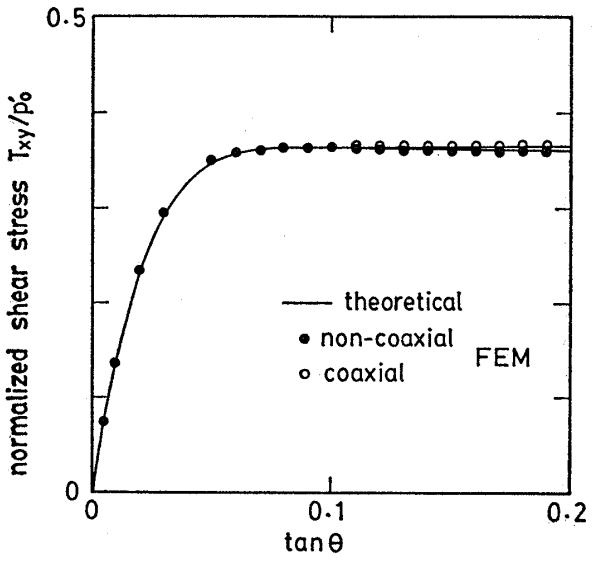

Fig. 3(b). Shear stress for a simple shear test

ness of SHEBLA for practical problems.

SHEAR BANDS FORMATION IN A PUNCH PROBLEM

Here we apply SHEBLA to a classical problem, so-called 'punch problem'. We do this by employing the constant strain quadrilateral element consisting of 4 nodes, and define the total water head at the center of the element. Fig. 4 shows the geometry of the analytical region. Particularly in relation to the width of the footing, this region should be large enough and also should be divided into finer finite element meshes. However, we determine the geometry of the analytical region here by taking the capacity of the computer and the availability of the computation costs into consideration,

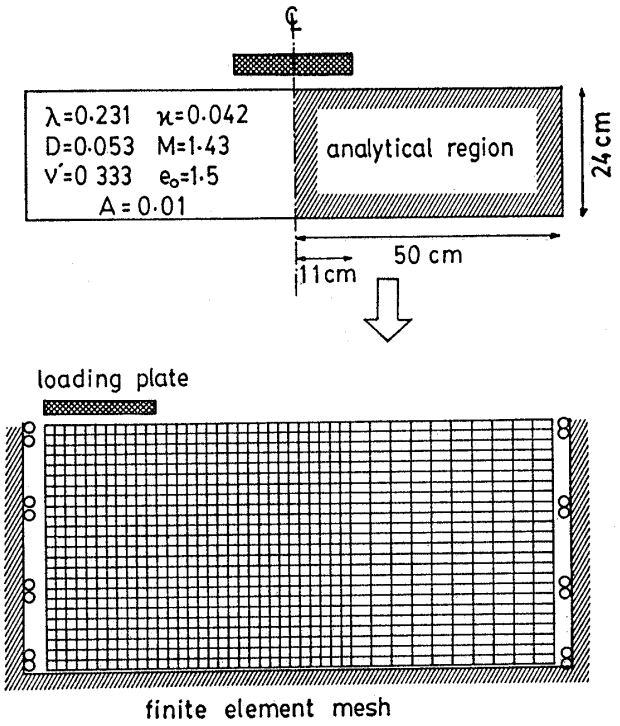

Fig. 4. Geometry of the analytical region and finite element meshes

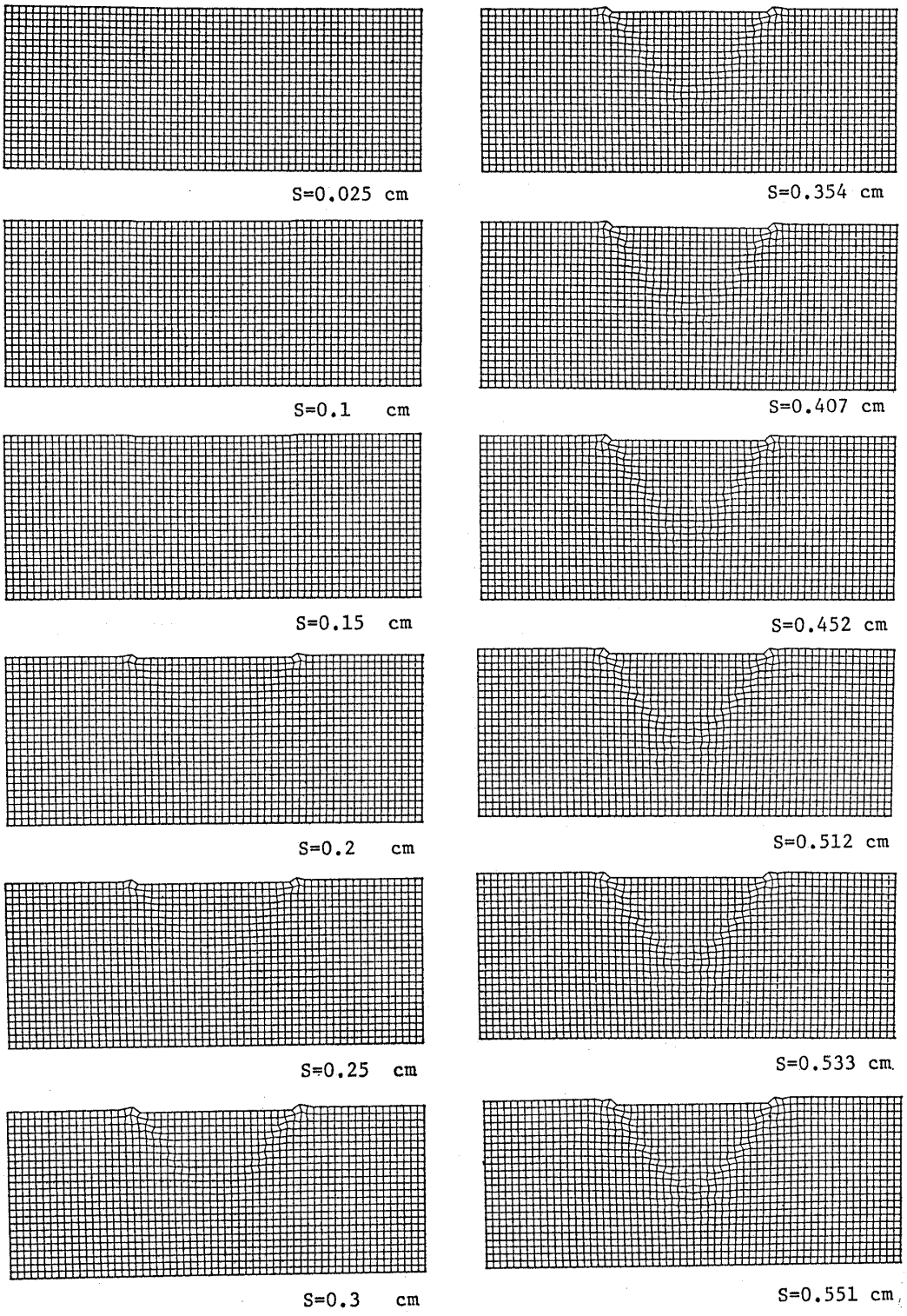

Fig. 5. The formation of shear bands

since our major purpose in conducting this analysis is to show the principles of shear bands formation rather than to solve the punch problem correctly. Due to kinematic symmetry, we actually employed the right hand region in the computations. The lower figure in Fig. 4 displays the finite element mesh in the present calculations. The analysis is carried out under the plane strain conditions. We assume a rough interface

between the rigid loading plate and the ground surface, so that the ground surface beneath the loading plate can only move vertically. Thus, the boundary conditions under the loading plate are given by the settlements, and the other locations on the upper boundary are stress free. The bottom boundary is fixed in all directions, while the side boundaries are fixed in only the horizontal direction, such that the vertical displacement is allowed (Appendix). The ground is assumed to be homogeneous; therefore, no initial imperfections are introduced into the material elements. The initial conditions are $p'=1.0\,\mathrm{kgf/cm^2}$ and $u=0$ at any point in the material. The same material parameters are used in our last paper (Yatomi et al., 1989) and $A=0.01$ is assumed in the present calculations. It should be noted here that shear bands localization could not be observed in the coaxial Cam-clay model, in which $A=0$.

Fig. 5 shows the process of formation for shear bands in the ground. Around the settlement $S=0.3$ cm, the localized shear deformation of the element just beneath the edge of the loading plate becomes significant, and the distorted elements link together in a downward direction as the settlement increases. At $S=0.551$ cm, the shear bands are easily recognized as the localized deformation of finite element meshes. After the shear bands reach the symmetric axis, they seem to extend on further to the right and the left directions. The deformed pattern in the last figure is very similar to the classical slip line solution obtained by Prandtl.

The hahavior of shear bands formation can be seen more clearly in a strain distribution. Fig. 6 shows the contour lines of the normalized strain defined by $\|\varepsilon\|=\sqrt{tr(\varepsilon\varepsilon^T)}$, in which $\varepsilon=\int_0^t \boldsymbol{D}dt$. In Fig. 6, the prominently localized zones of the normalized strain occur just beneath the edge of the loading plate and advance downward to the symmetric axis. Then they extend to both sides, in the same fashion as the shear bands formation in Fig. 5.

The relationship between the applied footing stress and the settlement of the loading plate is shown in Fig. 7. In this

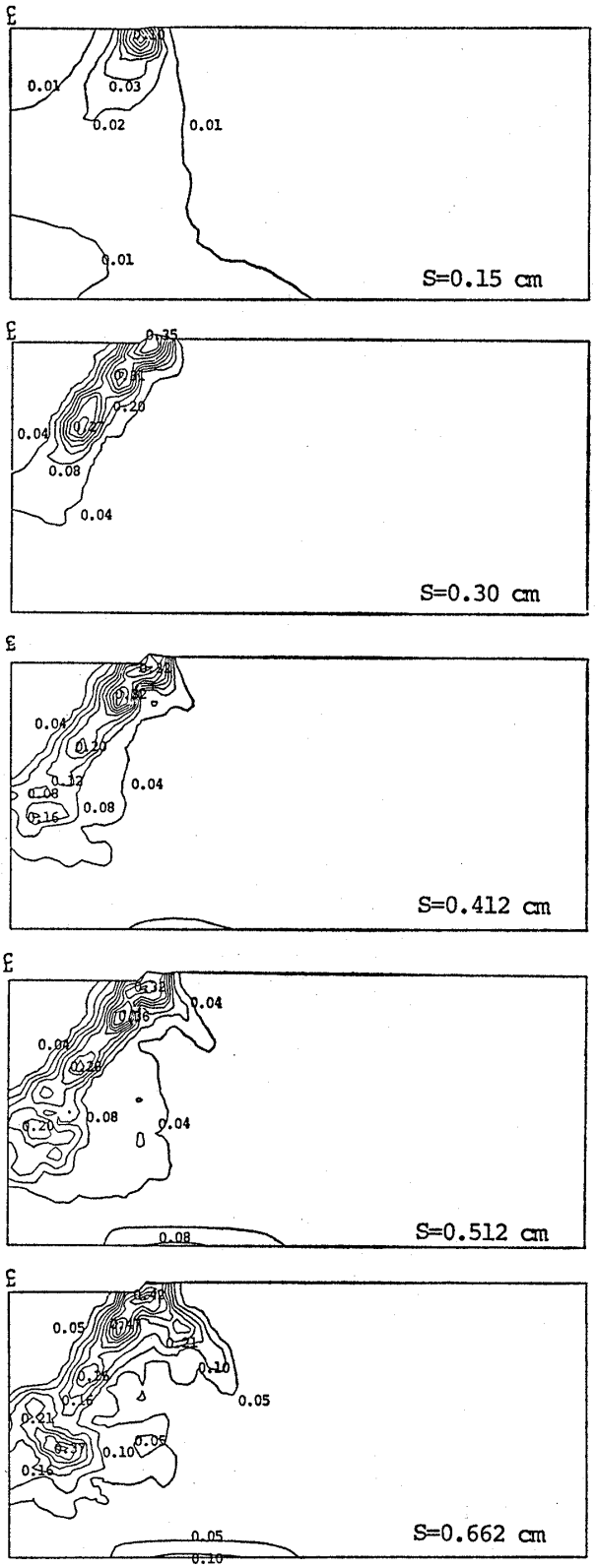

Fig. 6. The distribution of normalized strain

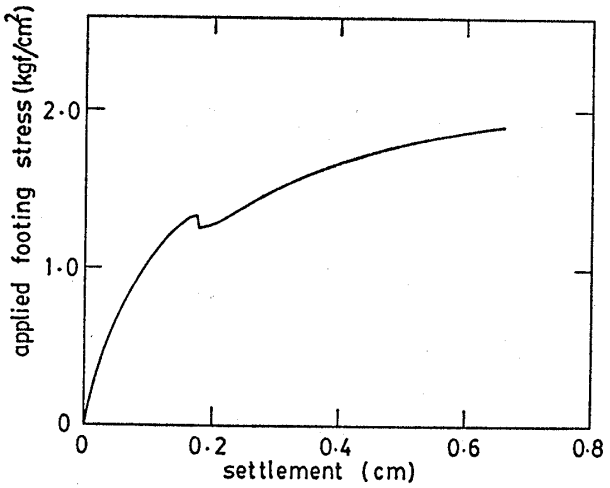

Fig. 7. The relationship between the applied footing stress and the settlement

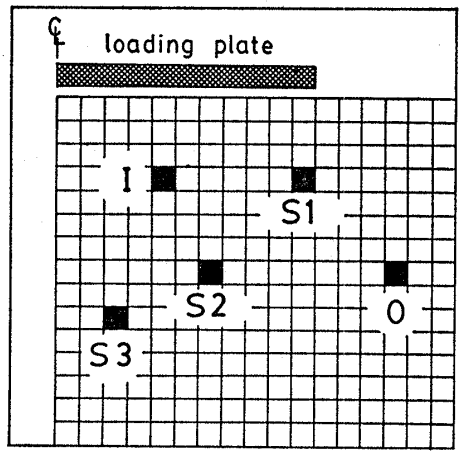

Fig. 8. The elements chosen for the trajectory path and the effective stress path

figure, the ultimate bearing capacity is not recognized and the applied footing stress exceeds the bearing capacity obtained by Prandtl's solution for small strains. This is probably due to the fact that the bottom boundary affected the shear bands formation and raised the bearing capacity, since the region analyzed in this computation was not deep enough. In this case, the ultimate bearing capacity by the Prandtl's solution is calculated as 1.87 kgf/cm² using the equation of undrained strength under the plane strain conditions proposed by Ohta et al. (1985). A small drop is observed around $S=0.175$ cm. This point corresponds to the settlement at which the stress state of an element reaches the critical state. Although the critical state need not be considered in the theoretical framework of finite strains, the Cam-clay model used here still has the critical state at which the model shows perfectly plastic behavior. In fact, the existance of a few critical elements dose not produce any instability in the numerical calculations.

Next, we shall discuss the trajectory path in the characteristic regimes for the five typical elements in Fig. 8 at each step of the settlement. The trajectory paths derived by both theory and the finite element method are shown in Fig. 9. The solid line in each figure represents the theoretical trajectory. It is found that elements S 1, S 2, and S 3 travel from the elliptic region (E) through the hyperbolic region (H) and finally reach the parabolic region (P). But each element passes the E-H boundary at a different time. Although the shear bands occur for the first time just beneath the edges of the loading plate (see Fig. 5), the element S 3 passes the E-H boundary long before the element S 1. On the other hand, elements I and O do not pass the E-H boundary, but remain in the elliptic region.

Fig. 10 shows the effective stress path in the p' vs. q stress space for each element. Elements S 1, S 2, and S 3 finally reach the critical state, but both element I (in the wedge surrounded by the shear bands) and element S 1 experience unloading once during the extension of the shear bands.

Figs. 11(a), (b), and (c) show the distributions of footing stress at $S=0.10$ cm, 0.35 cm, and 0.551 cm, respectively. It is clear that the stress initially becomes larger from the center axis to the edge of the loading plate, but finally becomes almost uniformly constant under the loading plate at the failure state. This behavior coincides with the empirical results for cohesive soils.

CONCLUDING REMARKS

We offer the following remarks as some

conclusions to the present paper.

1) Assuming Darcy's law for the motion of pore fluid, we summarized the governing equations for the coupling problem based on the finite strain theory.

2) We derived the finite element formulation by discretizing the governing equations based on the updated Lagrangean scheme. The program created here is called SHEBLA.

3) Without introducing any imperfections into the material elements, we demonstrated the formation of shear bands in the ground for the punch problem as the deformation of

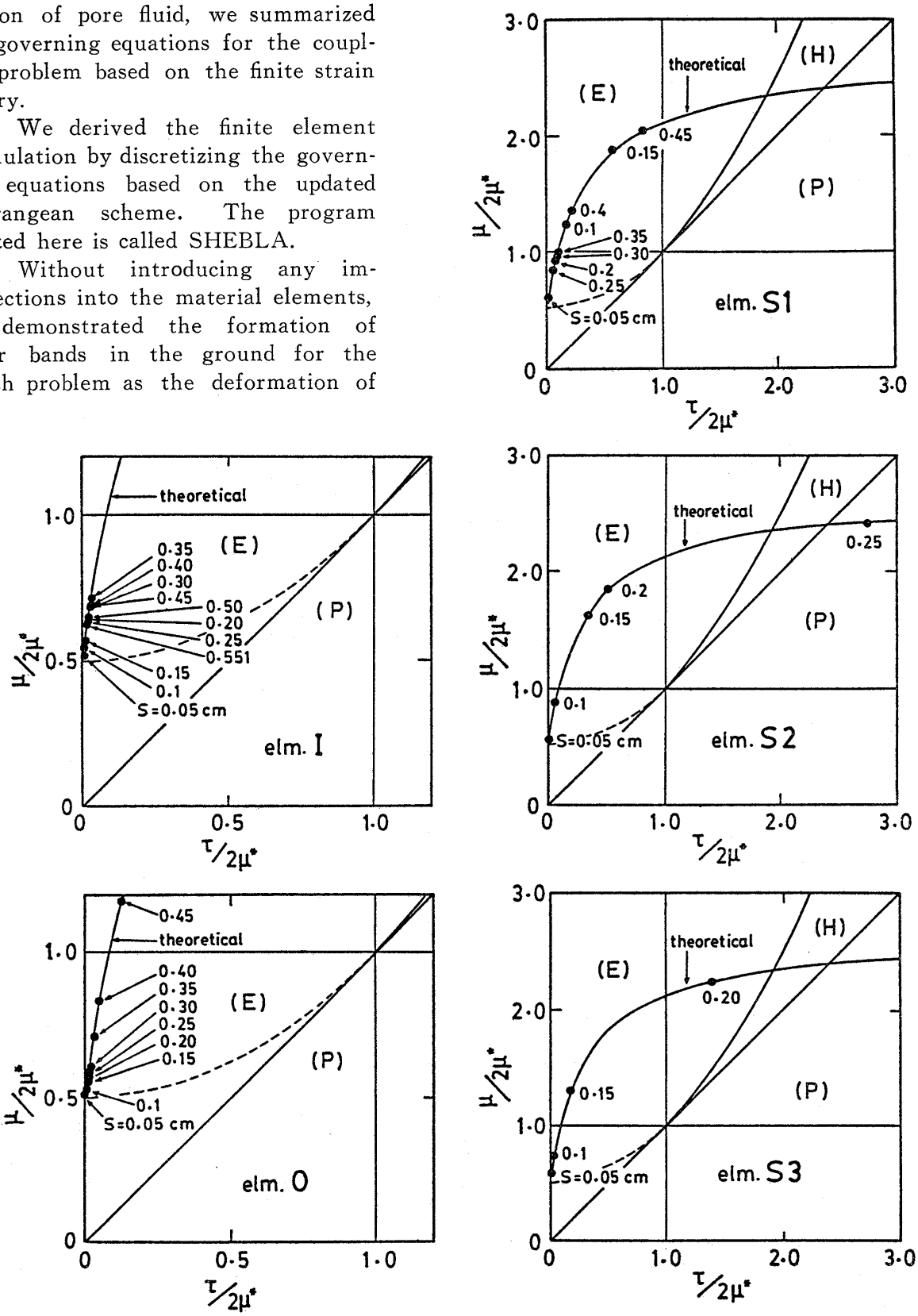

Fig. 9. The trajectory path in the characteristic regime

finite element meshes and also as the localized strain distribution.

4) Observing the process for the formation of shear bands, we found that the shear bands occur for the first time just around the edge of the loading plate and extend towards the symmetric axis. The stress state of the elements which form the shear bands reaches the hyperbolic region and then finally the parabolic region. The element in which a shear band occurs first, however, does not necessarily pass the *E–H* boundary first.

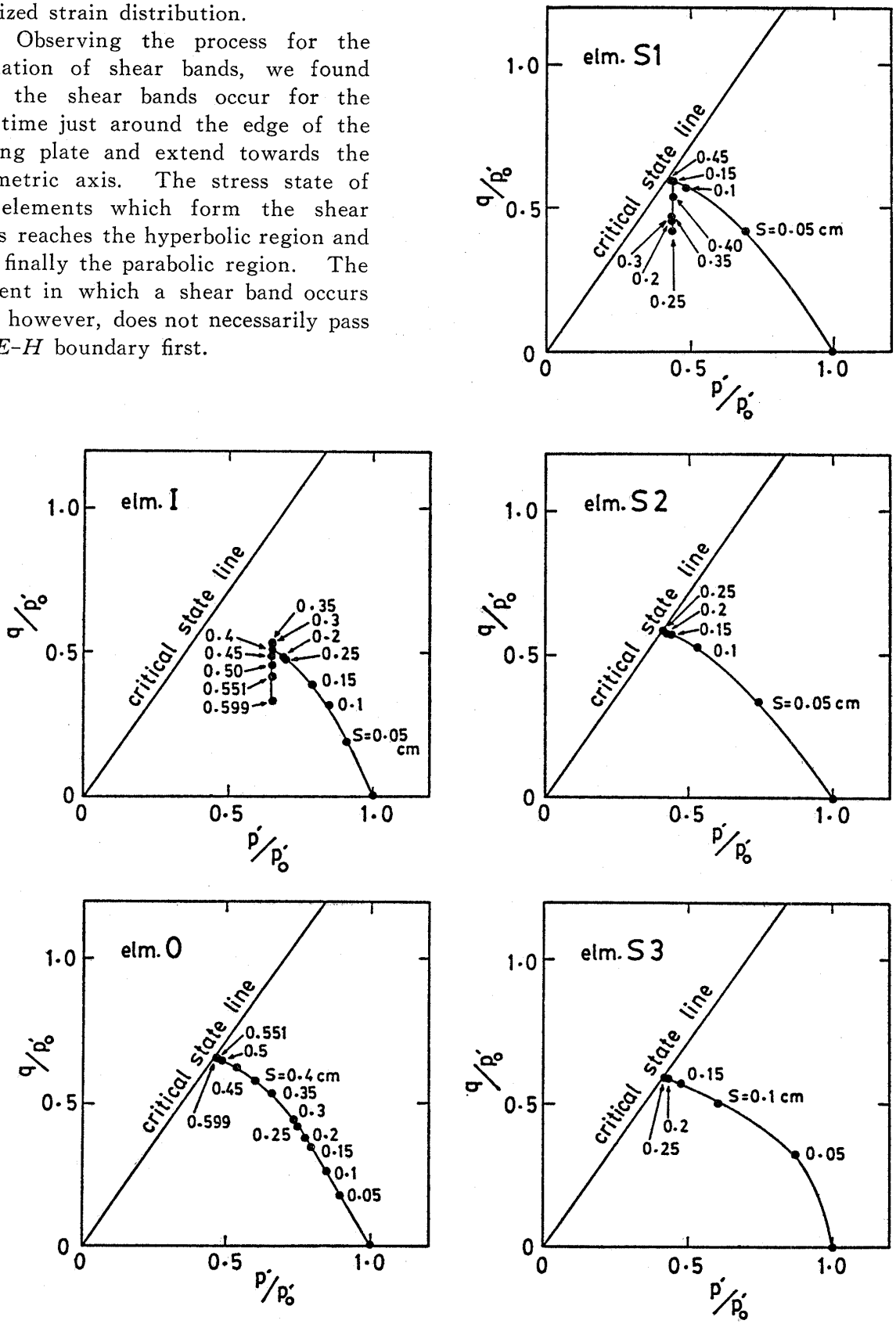

Fig. 10. The effective stress path in the p' vs. q stress space

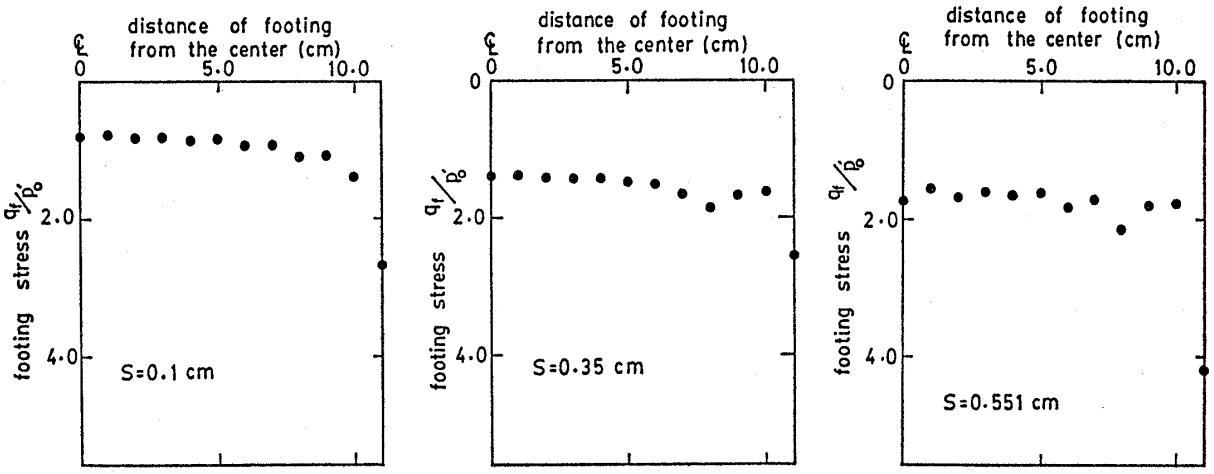

Fig. 11. The distribution of footing stress at each step

5) Observing the effective stress path, we discovered that both the element in the wedge surrounded by the shear bands and the element just beneath the loading plate experience unloading once during the extension of the shear bands.

6) And finally, we found that the distribution of footing stress at each step is similar to the empirical results for cohesive soils.

ACKNOWLEDGMENTS

We wish to express our gratitude for the encouragement received from Professor Hideki Ohta of Kanazawa University. We also wish to express our thanks to Mr. Sumio Sawada of Osaka Geo Research Institute. This study was supported in part by a Grant-in-Aid for Science Research, Project No. 63302045 from the Ministry of Education, Science and Culture. The numerical computations were performed at Kyoto University, Data Processing Center ; FACOM M 382 and VP 100.

NOTATIONS

$[B]$=matrix related as $\{D\}=[B]\{v^N\}$
$[B_G]$=matrix related as $\gamma_w\dot{\Omega}=[B_G]\{v^N\}$
$[B_v]$=matrix related as $tr\boldsymbol{D}=[B_v]\{v^N\}$
$[C]$=constitutive stiffness matrix
$\boldsymbol{D}$=stretching tensor
h=hardening modulus
h_1=second hardening modulus
h_w=total head of pore water
$\boldsymbol{K}$=permeability tensor
$\boldsymbol{L}$=velocity gradient
$[M]$=matrix related as $\{L\}=[M]\{v^N\}$
$[N]$=shape matrix
$\dot{\boldsymbol{S}}_t, \dot{\boldsymbol{S}}'_t$=total and effective nominal stress-rate
$\boldsymbol{T}, \boldsymbol{T}'$=total and effective Cauchy stress tensor
$\mathring{\boldsymbol{T}}'$=co-rotational rate of effective stress tensor
u=pore water pressure
$\{v\}$=velocity vector
$\{v^N\}$=velocity vector at a nodal point
$\{\Delta d\}$=increment of nodal displacements
$\{\Delta F\}$=load vector
η=stress ratio defined as q/p', in which
$q=\sqrt{3/2}\|\boldsymbol{S}\|$
Ω=potential head

REFERENCES

1) Akai, K. and Tamura, T. (1978) : "Numerical analysis of multi-dimensional consolidation accompanied with elasto-plastic constitutive equation," Proc. JSCE, No. 269, pp. 95-104 (in Japanese).
2) Biot, M. A. (1956) : "General solutions of the equations of elasticity and consolidation," Journal of Applied Physics, Vol. 78, pp. 91-96.
3) Christian, J. T. (1968) : "Undrained stress distribution by numerical method," Proc. ASCE, Vol. 94, SM 6, pp. 1333-1345.
4) Christian, J. T. and Boehmer, J. W. (1970) : "Plane strain consolidation by finite elements," Proc. ASCE, Vol. 96, SM 4, pp. 1435-1457.
5) Iizuka, A. and Ohta, H. (1987) : "A determination procedure of input parameters in elasto-viscoplastic finite element analysis," Soils and

Foundations, Vol. 27, No. 3, pp. 71-87.
6) Kikuchi, F. (1983) : "Finite element approximation and mathematical theory, incompressible viscous fluid," Suurikagaku, No. 236, Kyoritsu-Shuppan, pp. 7-13, (in Japanese).
7) Nagtegaal, J. C., Parks, D. M. and Rice, J. R. (1974) : "On numerically accurate finite element solutions in the fully plastic range," Comp. Meth. Appl. Mech. Eng., Vol. 4, pp. 153-178.
8) Ohta, H., Nishihara, A. and Morita, Y. (1985) : "Undrained stability of K_0-consolidated clay," Proc. 11 th ICSMFE, San Francisco, Vol. 2, pp. 613-617.
9) Prevost, J. H. (1984) : "Localization of deformations in elastic-plastic solids," Int. J. for Numerical and Analytical Methods in Geomechanics, Vol. 8, pp. 187-196.
10) Yatomi, C. and Nishihara, A. (1984) : "Principles of constitutive equations and expressions of anisotropy in soil materials," Soils and Foundations, Vol. 24, No. 3, pp. 15-26.
11) Yatomi, C., Yashima, A., Iizuka, A. and Sano, I. (1989) : "General theory of shear bands formation by a non-coaxial Cam-clay model," Soils and Foundations, Vol. 29, No. 3, pp. 41-53.

APPENDIX

The boundary conditions are summarized in Fig. A 1.

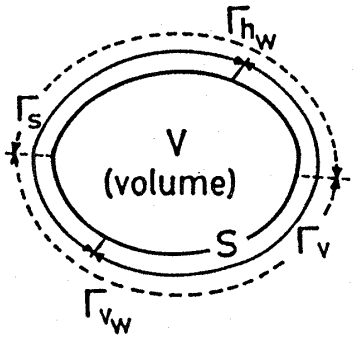

Fig. A 1. The boundary conditions of the coupling problem

$S=\Gamma_s+\Gamma_v$ (kinematic boundary),
and $S=\Gamma_{h_w}+\Gamma_{v_w}$(drainage boundary),
where S is the surface boundary of a region V at some given time t, and Γ_s, Γ_v, Γ_{h_w}, and Γ_{v_w} are subject to the total nominal traction-rate, the (displacement) velocity, the total water head, and the water velocity flowing outward, respectively. On these boundaries we need the known values as follows :

$$\bar{\dot{\boldsymbol{s}}}=\dot{\boldsymbol{S}}_t\boldsymbol{n} \quad (\text{on } \Gamma_s),$$
$$\bar{\boldsymbol{v}}=\boldsymbol{v} \quad (\text{on } \Gamma_v),$$
$$\bar{h}_w=h_w \quad (\text{on } \Gamma_{h_w}),$$
and $$\bar{\boldsymbol{v}}_w=\boldsymbol{K}\cdot grad(h_w) \quad (\text{on } \Gamma_{v_w}),$$

In our simulation of a 'punch problem', the Cauchy traction $\boldsymbol{t}$ and its rate $\dot{\boldsymbol{t}}$ are equal to zero on the free surface (Γ_s). Therefore, the nominal traction-rate on its boundary is $\bar{\dot{\boldsymbol{s}}}=\boldsymbol{0}$, since $\dot{\boldsymbol{s}}=\dot{\boldsymbol{t}}+(tr\boldsymbol{D}-\boldsymbol{n}\cdot\boldsymbol{D}\boldsymbol{n})\boldsymbol{t}$. On the other hand, the drainage boundary in our simulation is assumed to be impermeable ($\bar{\boldsymbol{v}}_w=\boldsymbol{0}$) in order to fulfill the perfect undrained conditions.